Advances in Applied Mathematics and Mechanics
Adv. Appl. Math. Mech., Vol. **1**, No. 6, pp. 799-815

DOI: 10.4208/aamm.09-m09S05
December 2009

Investigation of Taylor-Görtler-like Vortices Using the Parallel Consistent Splitting Scheme

Yong Hong Kuo[1,2], Kawi-Lam Wong[1,2] and Jeff Chak-Fu Wong[1,2,*]

[1] *The Joint Institute for Computational Sciences, University of Tennessee/Oak Ridge National Laboratory, Building 5100, RM 209, Mail Stop 6013, Bethel Valley Road, P.O. Box 2008 Oak Ridge, TN 37831-6013*

[2] *Department of Mathematics, Room 220, Lady Shaw Building, The Chinese University of Hong Kong, Shatin, Hong Kong*

Received 10 May 2009; Accepted (in revised version) 08 October 2009
Available online 18 November 2009

Abstract. Symmetric Taylor-Görtler-like vortices at Re=3200 and 5000 in 3D rectangular cavities with a moving top lid are studied numerically and tested with a spanwise aspect ratio of $1:1:L$, where L=1, 2, 3. Solutions are obtained by solving the momentum equations and the continuity equations using the consistent splitting scheme. The code presented here was ported to the Parallel Interoperable Computational Mechanics System Simulator (PICMSS). Stable solutions are obtained as limit cases of the transients.

AMS subject classifications: 65M10, 78A48

Key words: Mixed finite element, consistent splitting scheme, PICMSS.

1 Introduction

Numerical modelling of the three-dimensional (3D) flow of an incompressible viscous fluid in a 3D rectangular cavity with a moving wall is the most recognized test problem for verifying the accuracy and effectiveness of a numerical algorithm. Many researchers gave a comparative analysis of the solutions of the test problem in the GAMM workshop [6] in 1991 and reported that for moderate Reynolds number, say $Re \geq 3200$ for the spanwise aspect ratio (SAR) 1:1:3 the flow is essentially complex and unsteady. One of the most striking features of the flow pattern, known as the Taylor-Görtler-like (TGL) vortices, that were probably first found experimentally in [10], occurred in the transitive direction. Since then, many algorithms have been used for

*Corresponding author.
URL: `http://www.math.cuhk.edu.hk/~jwong`
Email: yonghongkuo@gmail.com (Y.-H. Kuo), wong@jics.utk.edu (K.-L. Wong), jwong@math.cuhk.edu.hk (J. C.-F. Wong)

finding supportive evidence for the appearance of TGL vortices, e.g. finite volume [3], finite difference [2], and lattice Boltzmann method [14].

In the present work, we report the results of a numerical integration with the mixed finite element (FE) formulation of the consistent splitting scheme (CSS), as proposed earlier by Shen and Guermond [8]. Based on our observations, with finer grid refinement, several pairs of symmetric TGL vortices are obtained and even better results are yielded. Parallel computing is an indispensable tool for producing long-time simulations of a large scale problem while increasing the degrees of freedom. The code developed here was ported to the Parallel Interoperable Computational Mechanics System Simulator (PICMSS) [15]. Our calculations have been performed by two choices of Reynolds numbers, Re=3200 and 5000, and three SARs of 1:1:1, 1:1:2 and 1:1:3. As we shall see below, not only are stable solutions obtained as limit cases of the transients, but also the behaviour of the pressure solution is free of node-to-node oscillations in this work.

The paper is divided into five sections; the first being the Introduction. Section 2 includes the general formulation of the problem and the physical problem with the boundary condition is described. Section 3 addresses the detailed numerical procedure for solving the 3D Navier-Stokes equations in the primitive variable form and the parallel computing engine, namely the PICMSS. Section 4 presents the results using the parallel mixed FE of the CSS solver and compares them with the other existing results. Section 5 gives the concluding remarks.

2 Formulation of the problem

The motion induced in a viscous incompressible fluid, contained in a 3D cavity of width W, length L and height H due to instantaneous motion of a sliding wall at a constant velocity is governed by the relation:

$$\frac{\partial \boldsymbol{u}}{\partial t} + (\boldsymbol{u}\cdot\nabla)\boldsymbol{u} = -\nabla p + \frac{1}{Re}\nabla^2\boldsymbol{u}, \qquad \text{in } \Omega\times(0,T], \tag{2.1}$$

$$\nabla\cdot\boldsymbol{u} = 0, \qquad \text{in } \Omega\times[0,T], \tag{2.2}$$

where $\boldsymbol{u}$=$\boldsymbol{u}(\boldsymbol{x},t)$=$(u,v,w)$ is the non dimensional velocity, p=$p(\boldsymbol{x},t)$ is the non-dimensional pressure, Re is the Reynolds number, t is the time, and $\boldsymbol{x}$=(x,y,z) is the spatial coordinate. A fixed final time is T. The bounded domain is

$$\Omega = [0,W]\times[0,L]\times[0,H].$$

Given an initial velocity field, which satisfies Eq. (2.2) and appropriate boundary conditions for $\boldsymbol{u}$, Eqs. (2.1) and (2.2) can be solved, in principal, for $\boldsymbol{u}$ and p as functions of space and time.

It is well-known that several pairs of Taylor-Görtler-like vortices, experimentally and numerically speaking, appear on the lower wall when the Reynolds number increases and the SAR of the cavity (Width:Height:Length = $W:H:L$) varies. The

analysis model is depicted in Fig. 1. All the walls of the cavity have no-slip boundary conditions except the top lid, which has the non-dimensional velocity of 1 in the x-direction. The cubic cavity initially occurs in motionless fluid, i.e., $u = v = w = 0$, and the initial pressure is zero. In the reference frame illustrated in Fig. 1, the boundary conditions are no-slip walls, given by

$$\boldsymbol{u}|_{\partial\Omega_{\text{Top}}} = (1,0,0), \qquad \text{and} \qquad \boldsymbol{u}|_{\partial\Omega-\partial\Omega_{\text{Top}}} = (0,0,0),$$

where $\partial\Omega$ is the boundary of Ω and $\partial\Omega_{\text{Top}}$ represents the top surfaces.

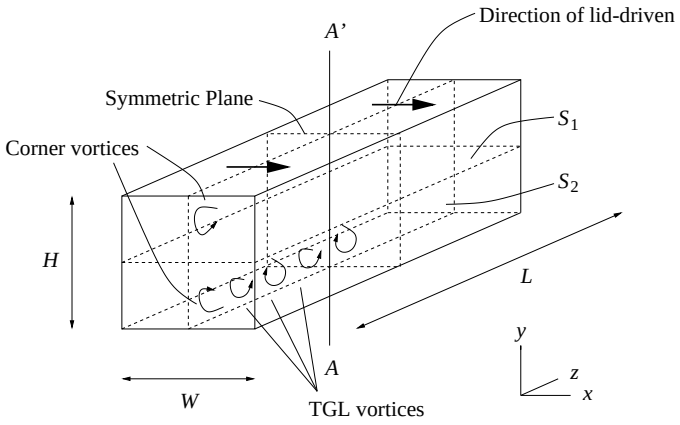

Figure 1: Geometry and boundary conditions for the 3D lid-driven cavity.

3 Numerical method & PICMSS

3.1 Consistent splitting scheme

Based on the Hodge-Helmholtz decomposition in conjunction with the pressure incremental scheme, velocity-pressure decoupling for solving a 3D rectangular cavity is achieved at Re=1000 and SAR 1:1:2 (see [7]). In order to further reduce the numerical boundary layer effect for the pressure, Shen and Guermond [8] proposed an efficient scheme for solving the velocities and pressure successfully for each time step, which they named the consistent splitting scheme. To the best of our knowledge, using the parallelization of the CSS for handling Re=3200 at various SAR cases is not an established practice yet.

Let us briefly describe the scheme here: The initial values

$$\boldsymbol{u}^0 = \boldsymbol{u}^{-1} = \boldsymbol{u}(\boldsymbol{x},0), \quad \text{and} \quad p^0 = p^{-1} = p(\boldsymbol{x},0),$$

are given. Let $(\boldsymbol{u}^n, p^n)$ be the n^{th}-order approximation to $(\boldsymbol{u}(\boldsymbol{x},n\Delta t), p(\boldsymbol{x},n\Delta t))$, where

Δt is the time-step size. For $n \geq 1$, find $\boldsymbol{u}^n$ and p^n such that

$$\begin{cases} \dfrac{\boldsymbol{u}^n - \boldsymbol{u}^{n-1}}{\Delta t} + (\boldsymbol{u}^{n-1} \cdot \nabla)\boldsymbol{u}^n + \dfrac{1}{2}(\nabla \cdot \boldsymbol{u}^{n-1})\boldsymbol{u}^n - \dfrac{1}{Re}\nabla^2 \boldsymbol{u}^n = -\nabla p^{n-1}, \\ \boldsymbol{u}^n|_{\partial\Omega} = \boldsymbol{b}^n. \end{cases} \tag{3.1}$$

$$(\nabla \phi^n, \nabla q) = -\left(\nabla \cdot \left(\frac{\boldsymbol{u}^n - \boldsymbol{u}^{n-1}}{\Delta t}\right), q\right), \qquad \forall q \in H^1(\Omega), \tag{3.2}$$

$$p^n = \phi^n + p^{n-1} - \frac{1}{Re}\nabla \cdot \boldsymbol{u}^n. \tag{3.3}$$

Remarks: (1) We use the first-order scheme in space, together with the backward Euler scheme in time. Error estimates for this scheme can be found in [13] (see Theorem 3.1). (2) The time integrator used in the momentum equation (see Eq. (3.1)) is fully implicit for the viscous term and semi-implicit for the nonlinear advection term. To avoid any restriction on the time step (i.e., to ensure unconditional stability), the advection term $\boldsymbol{u} \cdot \nabla \boldsymbol{u}$ has been replaced by its skew-symmetric counterpart (e.g., [7])

$$(\boldsymbol{u} \cdot \nabla)\boldsymbol{u} + \frac{1}{2}(\nabla \cdot \boldsymbol{u})\boldsymbol{u}.$$

(3) Of particular interest in Eq. (3.2) is that the auxiliary pressure ϕ^n, treated as a correction term, is unknown and will be determined at each time-step. (4) The pressure p^n in Eq. (3.3) is not only updated by the previous term p^{n-1} but also reduced down by the boundary layer effect among the bounded surface because of the term

$$\frac{1}{Re}\nabla \cdot \boldsymbol{u}^n.$$

3.2 Mixed FE formulation

Let $\mathcal{T}_h$ be a regular FE mesh consisting of hexahedral FE mesh. We define X_h, the approximation space for the velocity, as the set of continuous functions that are piecewise quadratic on each hexahedron of $\mathcal{T}_h$. The approximation space N_h for the auxiliary pressure and pressure consists of continuous functions that are piecewise linear on each hexahedron. To ensure that the auxiliary pressure and pressure are uniquely defined, we require it to have a mean value of zero.

The weak formulation of the advection-diffusion step Eq. (3.1) is: for $n \geq 1$, find $\boldsymbol{u}_h^n \in X_h$ with $\boldsymbol{u}_h^n|_{\partial\Omega} = \boldsymbol{b}_h^n$, such that

$$\begin{aligned} \left(\frac{\boldsymbol{u}_h^n - \boldsymbol{u}_h^{n-1}}{\Delta t}, \boldsymbol{v}_h\right) + \left((\boldsymbol{u}_h^{n-1} \cdot \nabla)\boldsymbol{u}_h^n + \frac{1}{2}(\nabla \cdot \boldsymbol{u}_h^{n-1})\boldsymbol{u}_h^n, \boldsymbol{v}_h\right) \\ + \frac{1}{Re}\left(\nabla \boldsymbol{u}_h^n, \nabla \boldsymbol{v}_h\right) = -\left(\nabla p_h^{n-1}, \boldsymbol{v}_h\right), \end{aligned} \tag{3.4}$$

for all $\boldsymbol{v}_h$ with $\boldsymbol{v}_h|_{\partial\Omega} = \boldsymbol{0}$.

The weak form of the two correction steps take the following forms: for $n \geq 1$, find $\phi_h^n \in N_h$ such that

$$(\nabla\phi_h^n, \nabla q_h) = -\Big(\nabla \cdot \Big(\frac{\boldsymbol{u}_h^n - \boldsymbol{u}_h^{n-1}}{\Delta t}\Big), q_h\Big), \tag{3.5}$$

and find $p_h^n \in N_h$ such that

$$(p_h^n, q_h) = \left(\phi_h^n + p_h^{n-1} - \frac{1}{Re}\nabla \cdot \boldsymbol{u}_h^n, q_h\right), \tag{3.6}$$

for all $q_h \in N_h$. The basic principle in the choice of FE base functions is to avoid node-to-node pressure oscillations that satisfy the *inf-sup* compatibility condition. The element pair used for the present work is a Hood-Taylor type (see e.g., [1]); u_h, v_h and w_h are interpolated in a quadratic fashion, while p_h and ϕ_h are interpolated in a linear manner, as depicted in Fig. 2.

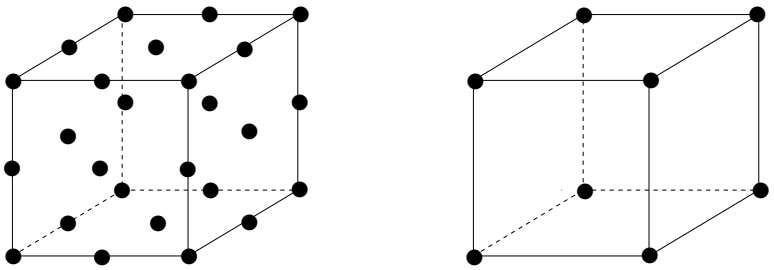

Figure 2: Mixed finite element method of hexahedral elements: 27/8 nodes.

By recalling the following result established in [13], we have:

Theorem 3.1. *Under convenient regularity assumptions on the data* $\boldsymbol{u}$ *and* $\boldsymbol{b}$*, and provided the inf-sup condition is satisfied, the solution to the first order CCS (Eqs.* (3.4)–(3.6)*) satisfies the error bounds*

$$\| \boldsymbol{u} - \boldsymbol{u}_h \|_{l^2(0,T;(H^1(\Omega))^3)} + \| p - p_h \|_{l^2(0,T;L^2(\Omega))} \leq c(h^l + \Delta t),$$

where c depends on $\boldsymbol{u}$ *and p, and l is the polynomial order of interpolation of velocity.*

3.3 PICMSS

PICMSS is a versatile implicit parallel FE computational engine built to solve large scale complex computation fluid dynamics (CFD) problems. PICMSS is capable of admitting various formulations of fluid flow simulations, directly written in partial differential equation (PDE) form, which makes it readily extensible to the CSS used in this paper. Some of its salient features are summarized as follows:

- An interface translates meshes generated by PATRAN or CUBIT to a set of parallel input data files.
- The computational kernel of PICMSS takes the input files and executes the problem statements defined in the equation file as written in PDE form.
- PICMSS provides a wide variety of options for FE types, time discretization schemes, choices of inner and outer iterations for multiple sets of linear and nonlinear equations, structured or unstructured mesh layouts, and many selections of sparse solvers and preconditioners.
- PICMSS is written in C language and MPI, hence it is widely portable.
- PICMSS adopts the Trilinos suites developed at the Sandia National Laboratory which is shown to be scalable on many supercomputer platforms.
- PICMSS writes out results in Tecplot and VTK formats. A user interface is also available to view the results using VISIT, a graphical tool freely available from Lawrence Livemore National Laboratory.

Until stated otherwise, we shall use the VISIT visualization software for analyzing all the flow physics.

4 Results and discussion

Until otherwise stated, the BiCGSTab Krylov sparse iterative solver, in conjunction with the least squares polynomial preconditioner, was selected to solve a system of matrix equations (see Eqs. (3.4) - (3.6)). Computations were carried out on the CRAY XT4 supercomputer at the Oak Ridge National Laboratory. For all the calculations, the uniform mesh-layout is used.

4.1 Numerical verification

The performance of the parallelized CSS on the accuracy of the numerical solutions is assessed against the following analytical test problem. The domain is $[0,\pi]^3$, and the exact solution of the problem is given, in dimensionless form, as

$$\begin{aligned} u(x,y,z,t) &= \sin x \sin(y+z+t),\\ v(x,y,z,t) &= \cos x \cos(y+z+t),\\ w(x,y,z,t) &= \cos x \sin(y+t),\\ p(x,y,z,t) &= \cos x \cos y \cos z \sin t. \end{aligned}$$

The nonzero values at T=0 were used as an initial condition for the Reynolds number of 40 with the final time T=1.

In Table 1 are the errors of the velocities and pressures in various norms. In the mixed FE technique, three different uniform grids,

$$G_1 : \frac{17^3}{9^3}, \quad G_2 : \frac{33^3}{17^3}, \quad \text{and} \quad G_3 : \frac{65^3}{33^3},$$

Table 1: Convergence results for velocities and pressures. h_0=$\max_{\widetilde{K}\in\mathcal{T}_h}\{h_{\widetilde{K}} : h_{\widetilde{K}} = \mathrm{diam}(\widetilde{K})\}\in G_1$, where $\widetilde{K}$ is a hexahedral element, and $\Delta t_0 = 0.1$ using the 27/8 hexahedral element pair with the first-order scheme in time.

Mesh types	Mesh sizes	Time steps	$\| u-u_h \|_{l^2(0,T;L^2(\Omega))}$	ratios	$\lvert u-u_h\rvert_{l^2(0,T;H^1(\Omega))}$	ratios
G_1	h_0	Δt_0	0.7793E-1	—	0.9486E00	—
G_2	$\frac{1}{2}h_0$	$\frac{1}{4}\Delta t_0$	0.2110E-1	0.2727	0.3378E00	0.3562
G_3	$\frac{1}{4}h_0$	$\frac{1}{16}\Delta t_0$	0.5542E-2	0.2491	0.1023E00	0.3029
Mesh types	Mesh sizes	Time steps	$\| v-v_h \|_{l^2(0,T;L^2(\Omega))}$	ratios	$\lvert v-v_h\rvert_{l^2(0,T;H^1(\Omega))}$	ratios
G_1	h_0	Δt_0	0.1131E00	—	1.3030E00	—
G_2	$\frac{1}{2}h_0$	$\frac{1}{4}\Delta t_0$	0.3270E-1	0.2490	0.4354E00	0.3342
G_3	$\frac{1}{4}h_0$	$\frac{1}{16}\Delta t_0$	0.8676E-2	0.2491	0.1212E00	0.2783
Mesh types	Mesh sizes	Time steps	$\| w-w_h \|_{l^2(0,T;L^2(\Omega))}$	ratios	$\lvert w-w_h\rvert_{l^2(0,T;H^1(\Omega))}$	ratios
G_1	h_0	Δt_0	0.7278E-1	—	0.3914E00	—
G_2	$\frac{1}{2}h_0$	$\frac{1}{4}\Delta t_0$	0.2324E-1	0.3193	0.1366E00	0.3490
G_3	$\frac{1}{4}h_0$	$\frac{1}{16}\Delta t_0$	0.6190E-2	0.2664	0.4101E-1	0.3003
Mesh types	Mesh sizes	Time steps	$\| p-p_h \|_{l^\infty(0,T;L^2(\Omega))}$	ratios	$\| p-p_h \|_{l^2(0,T;L^2(\Omega))}$	ratios
G_1	h_0	Δt_0	0.1011E00	—	0.5968E00	—
G_2	$\frac{1}{2}h_0$	$\frac{1}{4}\Delta t_0$	0.3229E-1	0.2481	0.2072E00	0.3472
G_3	$\frac{1}{4}h_0$	$\frac{1}{16}\Delta t_0$	0.8833E-2	0.2495	0.6048E-1	0.2919

were used, e.g., for the G_1 type, the cavity was regularly divided into 17 grid points in the each direction. For all the computations, the number of processors is set to 33. It can be seen that the $|\cdot|_{l^2(0,T;H^1(\Omega))}$-error norms of the approximate velocities and the $\|\cdot\|_{l^2(0,T;L^2(\Omega))}$-error norm of the approximate pressure are $\mathcal{O}(h^{1.7}+\Delta t)$ (note that the expected ratio should be of $\mathcal{O}(h^2+\Delta t)$), while the $\|\cdot\|_{l^2(0,T;L^2(\Omega))}$-error norms of the approximate velocities and $\|\cdot\|_{l^\infty(0,T;L^2(\Omega))}$-error norm of the approximate pressure are $\mathcal{O}(h^2+\Delta t)$.

4.2 Case studies

A numerical investigation has been provided for different geometric configurations of cavity and different choices of Reynolds numbers. A Dirichlet pressure boundary value is imposed in order to ensure the uniqueness of the auxiliary pressure and pressure solutions.

The numerical results are summarized as follows:

• 1 : 1 : 1 —The number of degrees of freedom for the velocity and pressure are 2,146,689 and 274,625, respectively. The final time is T=180 with Δt=0.005 at Re=3200.

From Figs. 3 and 4 we can see that the flow structures in the specified planes agree well with those in [4, 9, 12, 14], and three pairs of symmetric TGL vortices are clearly

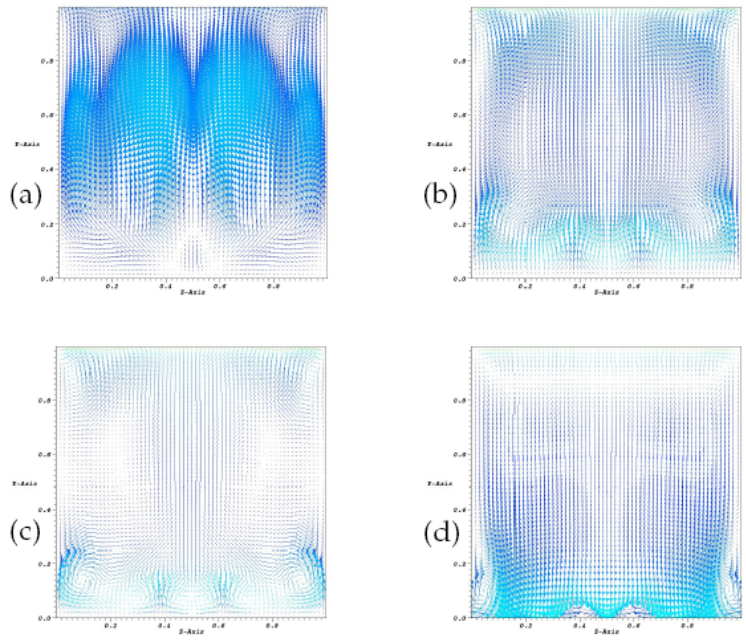

Figure 3: Velocity vectors on the y-z plane at (a) $x = 0.0625$, (b) $x = 0.375$, (c) $x = 0.5$ and (d) $x = 0.75$ for $Re = 3200$ at $1 : 1 : 1$.

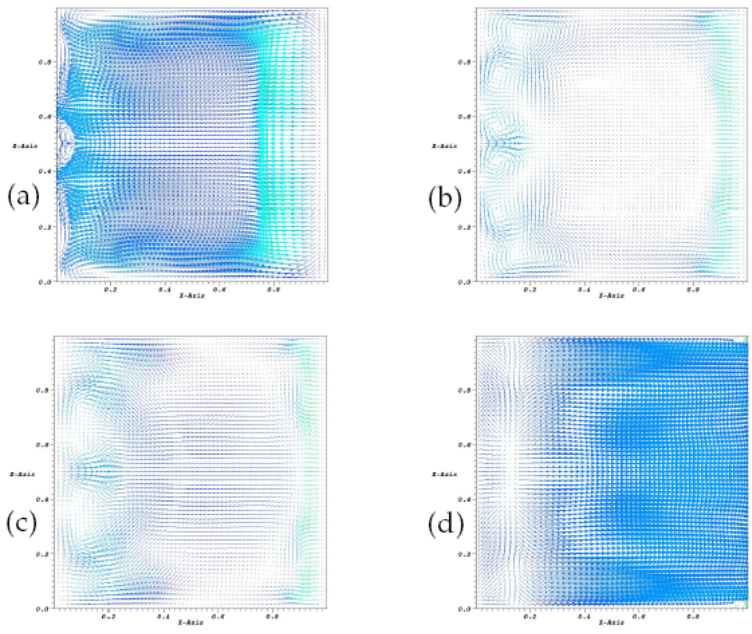

Figure 4: Velocity vectors on the x-z plane at (a) $y = 0.25$, (b) $x = 0.5$, (c) $x = 0.625$ and (d) $x = 0.9375$ for $Re = 3200$ at $1 : 1 : 1$.

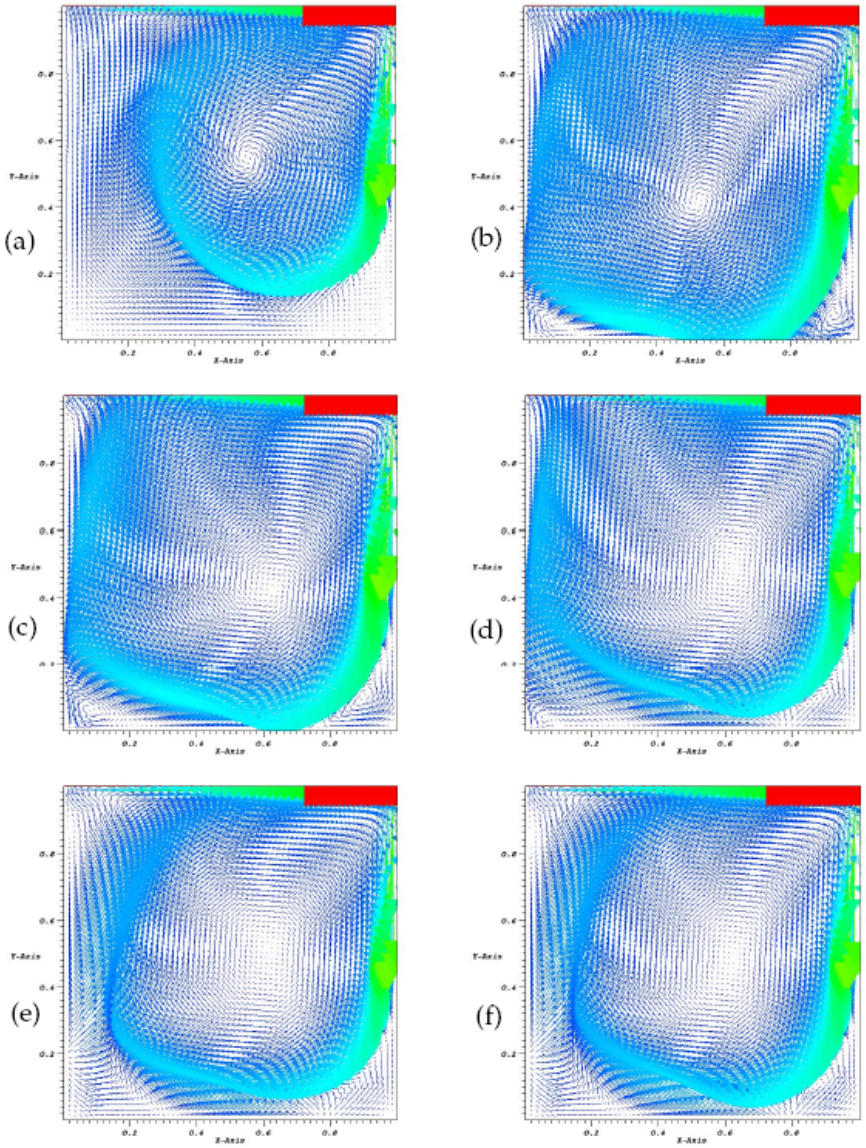

Figure 5: Velocity vectors on plane $z = 0.5$ at various time levels for $Re = 3200$, (a) $t = 12.5$, (b) $t = 24$, (c) $t = 32$, (d) $t = 48$, (e) $t = 84$, (f) $t = 180$.

visible along the spanwise direction as in [14].

Fig. 5 shows the x-component of the velocity on the $A - A'$ line (see Fig. 1). A primary vortex gradually grows bigger and bigger near the right corner of the top wall, and the center of the primary vortex moves to a location at about $(0.64, 0.49)$, while the downstream secondary vortex, upstream secondary vortex, and upper secondary vortex are also found in Fig. 5. Good agreement was found in the appearance of the primary as well as the corner vortices.

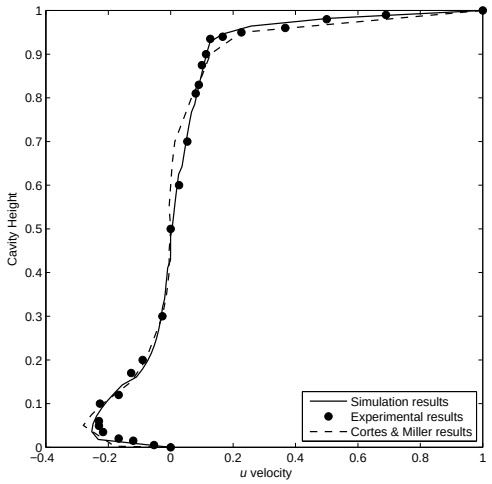

Figure 6: Comparison of the centerline velocity profile with the experimental and the existing results for a cubic cavity at $Re = 3200$.

Previous results from Koseff et. al. [11] and Cortes & Miller [5] are presented for comparison, as shown in Fig. 6. Good agreement was found in the u-velocity profile of the x-y plane (see S_1 plane in Fig. 1).

Similar to the TGL vortices, the formation, evolution and finally dissipation of the pressure solutions were found, as shown in Fig. 7. No unphysical oscillation was seen in the boundary wall of the cavity, except at the top lid corners.

• 1 : 1 : 2 — The number of degrees of freedom for the velocity and pressure are 4,276,737 and 545,025, respectively. The time-step size is Δt=0.01.

Re=3200. The transient solutions for Re=3200 are given at time levels T=18, 20, 25, 30, 35 and 40, as shown in Fig. 8. Inspection of these figures indicated that instantaneous velocity fields in a y-z plane (see S_2 plane in Fig. 1) from the downstream wall show the formation and evolution of seven symmetric pairs of TGL vortices in the whole cavity. Based on the reference [14], our results as shown in Fig. 10 (b), indicated that seven symmetric pairs of TGL vortices did occur at T=110. On the S_1 plane, several pairs of symmetric vortices are found in Fig. 10 (a). Upper and lower corner vortices are obtained as shown in Fig. 10 (b).

Similar to the TGL vortices, the formation, evolution and finally dissipation of the pressure solutions were found, as shown in Figs. 9 and 10 (c) - (d). It can also be seen that the tube-like pressure solutions gradually grow intense and move the geometric center of cavity with respect to the x-y plane. No spurious oscillation was seen in the boundary wall of the cavity, except near the top lid corners.

Re=5000. The transient solutions for Re=5000 at T=18, 20, 26, 30, 35 and 40 are shown in Fig. 11. Instantaneous velocity fields in the S_2 plane from the downstream wall also show the presence and evolution of seven symmetric pairs of TGL vortices, and a lower corner vortex at the end wall is seen. Comparison of Figs. 8(f) and 11(f)

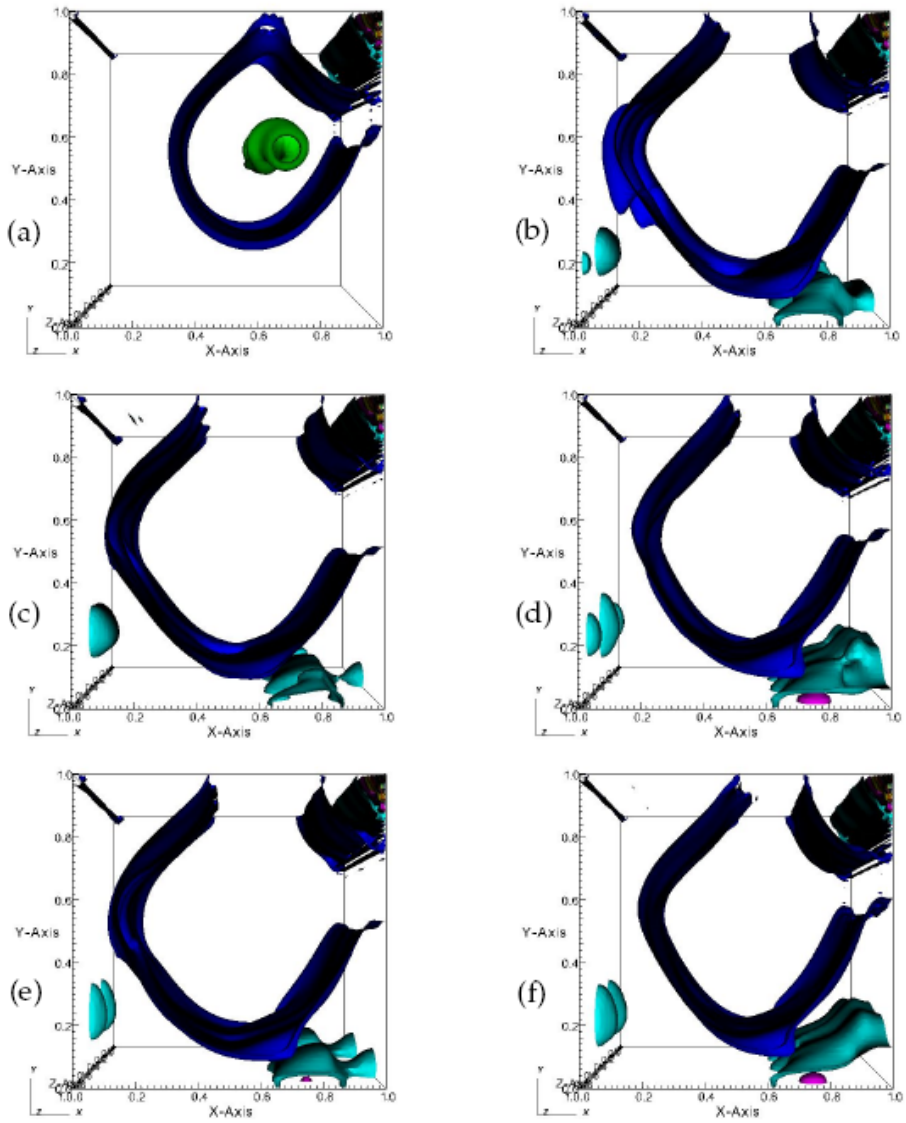

Figure 7: Pressure contour plots at various time levels for $Re = 3200$, (a) $t = 12.5$, (b) $t = 24$, (c) $t = 32$, (d) $t = 48$, (e) $t = 84$, (f) $t = 180$.

indicates that for the latter case, a pair of the TGL vortices burst out vividly at the vertical center line of the y-z plane, due to the influence of forced convection induced by the Reynolds number.

Similar to the results of Re=3000, Fig. 12 shows the formation, evolution and finally dissipation of the pressure solutions. No node-to-node oscillation was seen in the boundary wall of the cavity, except near the top lid corners.

• 1 : 1 : 3 — Let us summarize the computational cost and performance of this prob-

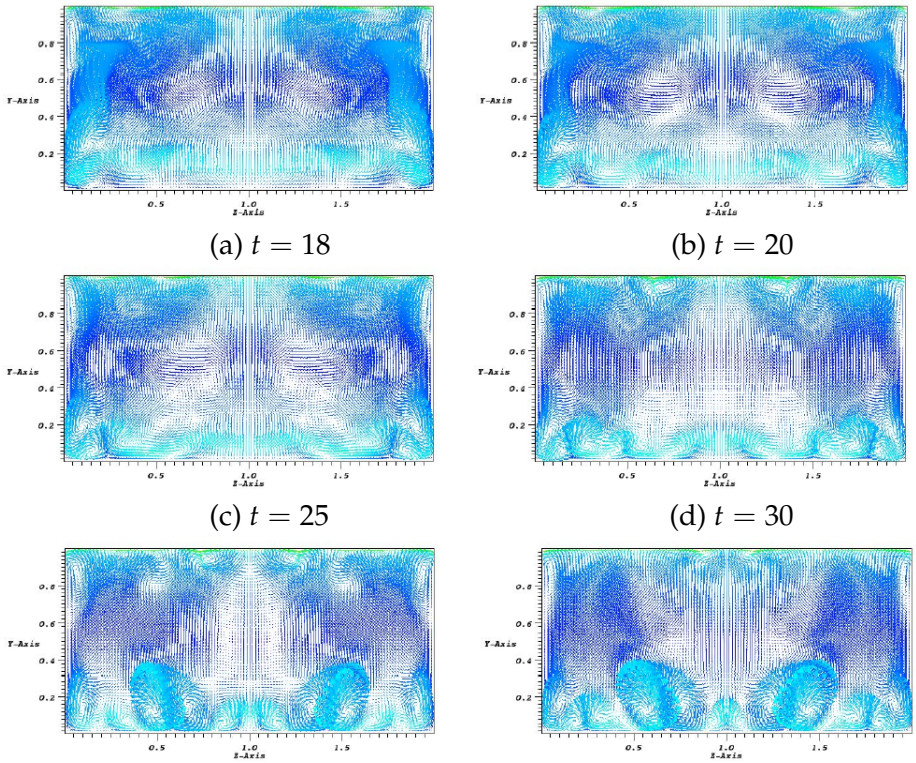

(a) $t = 18$ (b) $t = 20$

(c) $t = 25$ (d) $t = 30$

(e) $t = 35$ (f) $t = 40$

Figure 8: Velocity vectors on plane $x = 0.5$ at various time levels for $Re = 3200$ at $1:1:2$.

lem at Re=3200. The number of degrees of freedom for the velocity and pressure are 4,276,737 and 545,025, respectively. The time-step size is Δt=0.01.

Fig. 13 displays the transient solutions at $T = 40$. The flow structures in the specified planes are seen in Figs. 13 (a)-(b). Several pairs of symmetric TGL vortices are visible along the spanwise direction. In Fig. 13 (c)-(d), in particular, yet again, no node-to-node oscillation was seen at the boundary wall of the cavity, except near the top lid corners.

5 Concluding remarks

The CSS for the 3D incompressible Navier-Stokes equation and its parallel version has been established. The fluid flow at moderate Re can be simulated accurately and efficiently on finer uniform grids by the parallelized CSS, which is verified by the numerical tests of 3D lid-driven cavity problems for various Re and SAR. Some interesting observations were made:

- When the resolution was sufficiently high, a few pairs of symmetric TGL vortices

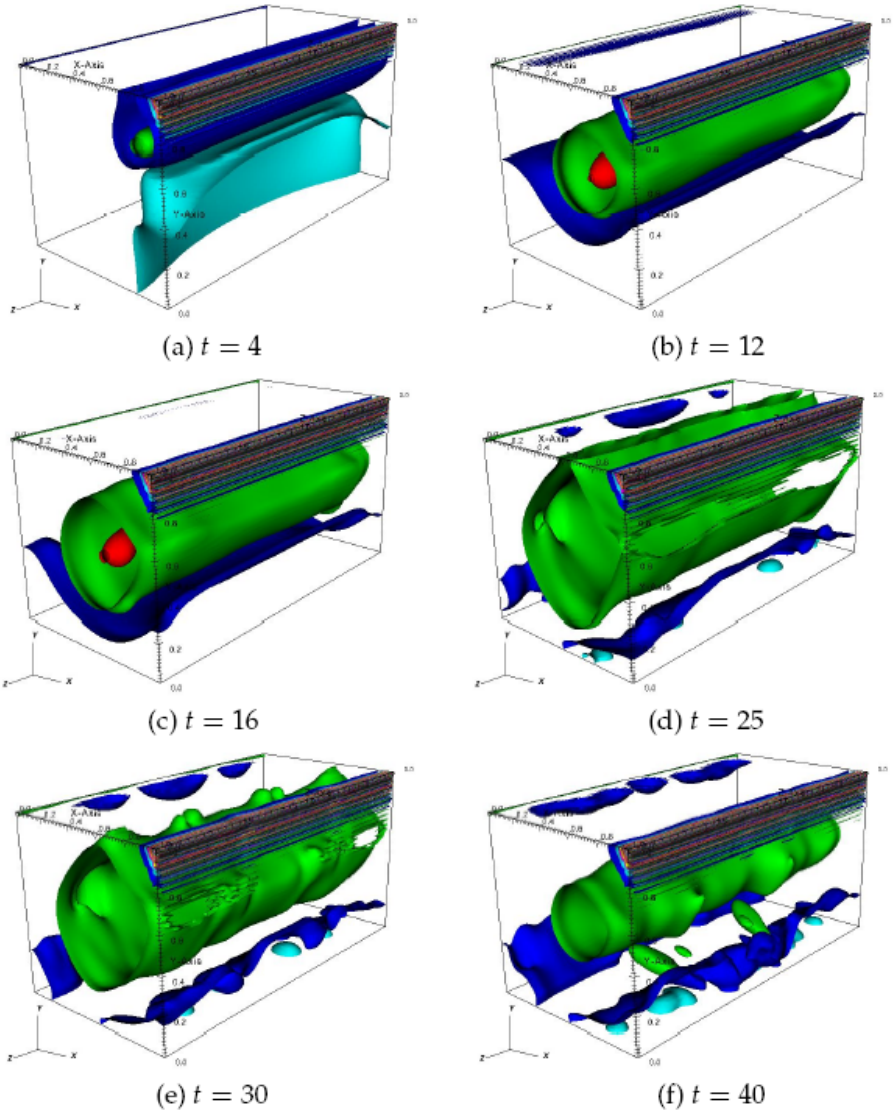

Figure 9: Pressure contour plots at various time levels for $Re = 3200$ at $1:1:2$, (a) $t = 4$, (b) $t = 12$, (c) $t = 16$, (d) $t = 25$, (e) $t = 30$, (f) $t = 40$.

were preserved.

- The pressure solutions are free of oscillation in the work, except at the corner of the sliding wall as expected.

There is more work to be done on the subject of the long time simulation of fluid flow problems at various choices of Reynolds numbers (e.g., ≥ 3200) and SARs. Our present results also indicated that using the non-uniform mesh layouts (e.g., using very dense grids near the boundary walls), the oscillating pressure solutions on the corners of the sliding wall would be reduced. These results will be reported elsewhere.

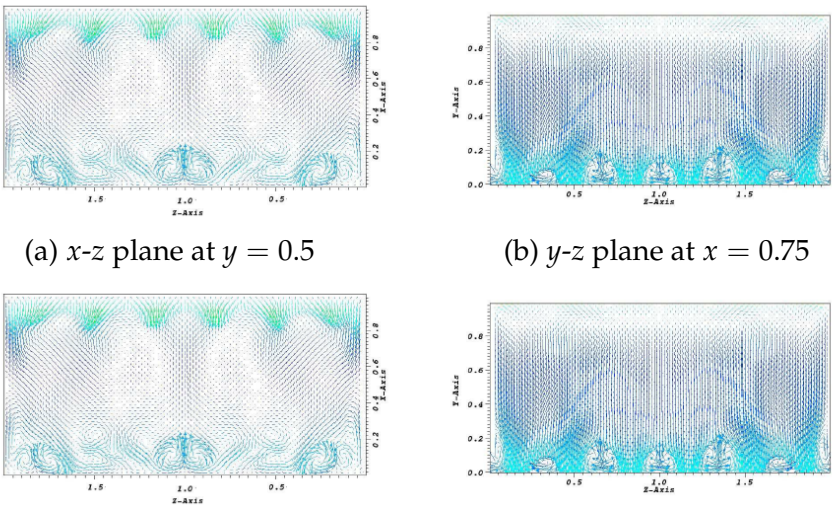

(a) x-z plane at $y = 0.5$ (b) y-z plane at $x = 0.75$

(c) Pressure (d) Pressure

Figure 10: Velocity vectors on the x-z plane at $y = 0.5$ and on the y-z plane at $x = 0.75$, and pressure contour plots for $Re = 3200$ at $1:1:2$ and at $T = 110$.

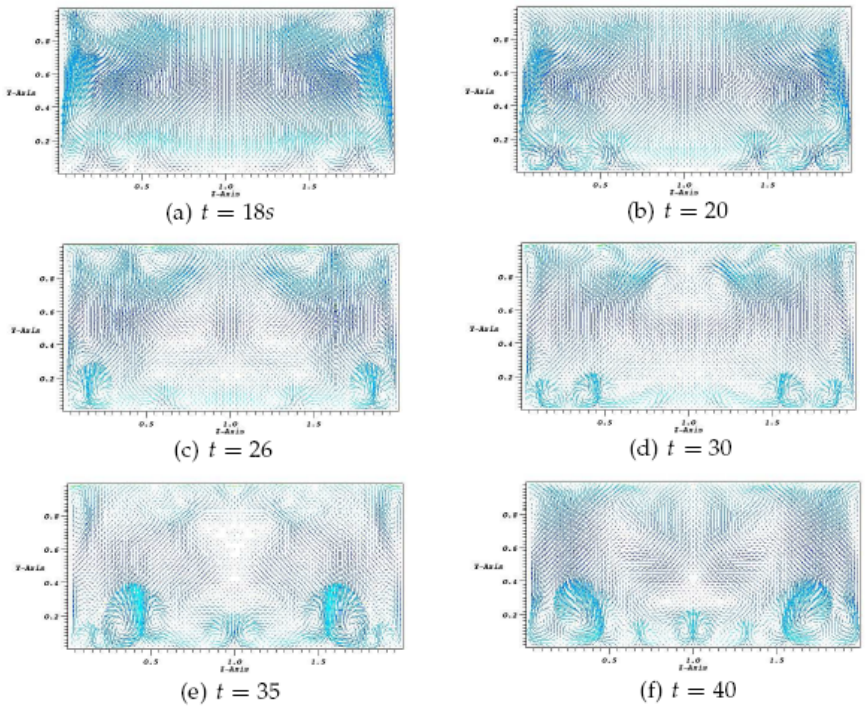

(a) $t = 18s$ (b) $t = 20$

(c) $t = 26$ (d) $t = 30$

(e) $t = 35$ (f) $t = 40$

Figure 11: Velocity vectors on plane $x = 0.5$ at various time levels for $Re = 5000$ at $1:1:2$, (a) $t = 18$, (b) $t = 20$, (c) $t = 26$, (d) $t = 30$, (e) $t = 35$, (f) $t = 40$.

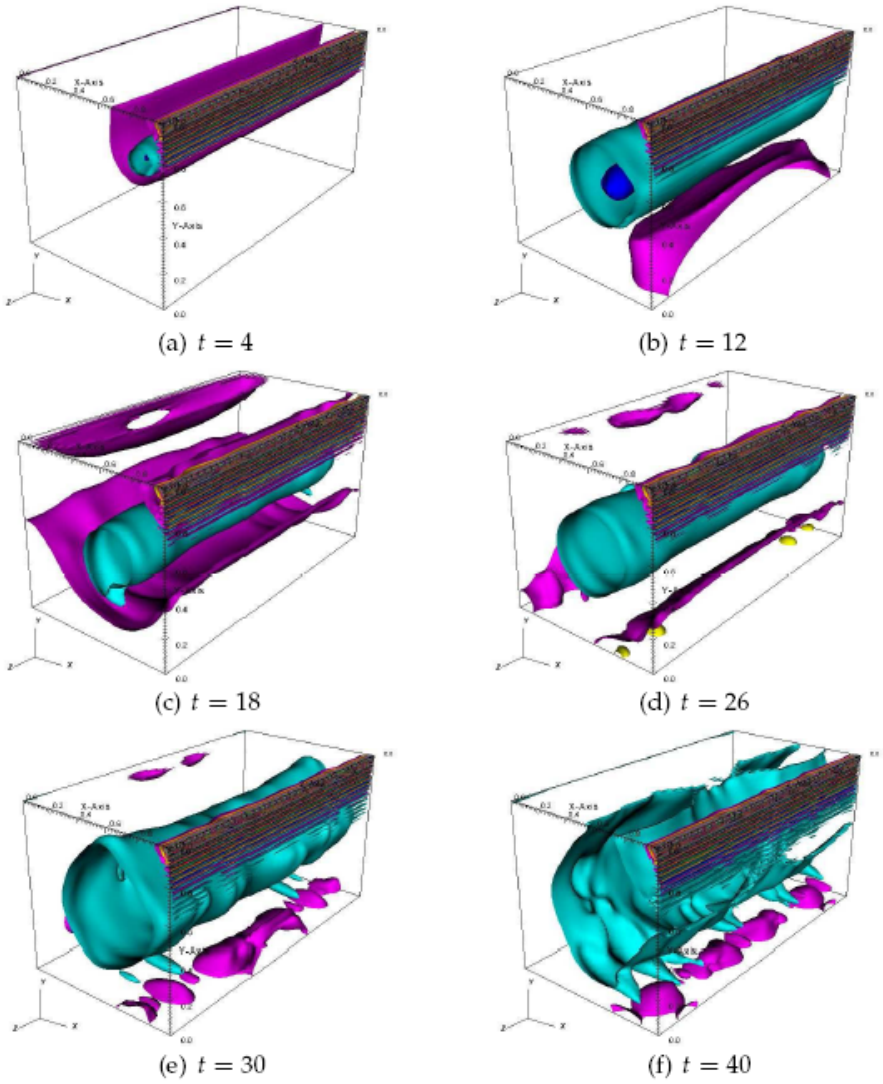

Figure 12: Pressure contour plots at various time levels for $Re = 5000$ at $1:1:2$.

Acknowledgments

The authors would like to thank the referees for the helpful suggestions. This research was supported by an allocation of advanced computing resources supported by the National Science Foundation. The computations were performed on Kraken and Athena (Cray XT) at the National Institute for Computational Sciences (`http://www.nics.tennessee.edu/`). K. H. Kuo's summer internship was partially support by CUHK and was supported/hosted by the Joint Institute for Computational Sciences at University of Tennessee/ Oak Ridge National Laboratory.

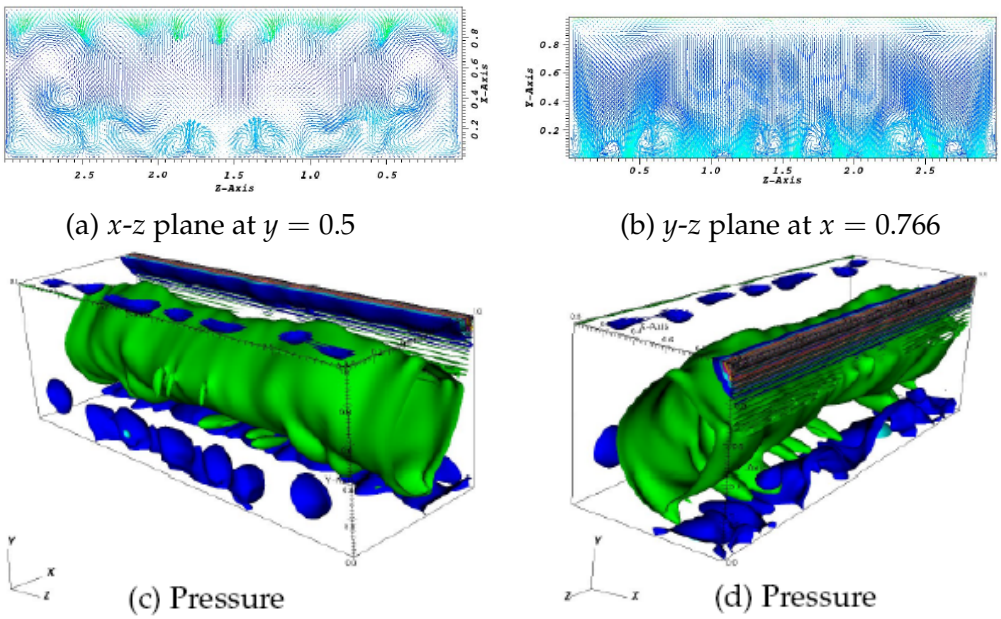

(a) x-z plane at $y = 0.5$ (b) y-z plane at $x = 0.766$

(c) Pressure (d) Pressure

Figure 13: Velocity vectors on the x-z plane at $y = 0.5$ and on the y-z plane at $x = 0.766$, and pressure contour plots for $Re = 3200$ at $1:1:3$ and at $T = 40$.

References

[1] K. J. BATHE, Finite Element Procedures, Prentice Hall, 1996.

[2] O. A. BESSONOV, V. A. BRAILOVSKAYA AND B. ROUX, *Numerical modeling of three-dimensional shear flow in a cavity with moving lids*, Fluid Dyn., 33 (1998), pp. 331–337.

[3] T. P. CHIANG AND W. H. SHEU, *Numerical prediction of eddy structure in a shear-driven cavity*, Comput. Mech., 20 (1997), pp. 379–396.

[4] T. P. CHIANG, W. H. SHEU AND R. R. HWANG, *Effect of Reynolds number on the eddy structure in a lid-driven cavity*, Int. J. Numer. Meth. Fluids, 26 (1998), pp. 557–579.

[5] A. B. CORTES AND J. D. MILLER, *Numerical experiments with the lid driven cavity flow problem*, Comput. & Fluids, 23 (1994), pp. 1005–1027.

[6] M. DEVILLE *et al.* (ed.), *Numerical simulation of 3D incompressible unsteady viscous laminar flows: A GAMM workshop*, Notes on Numerical Fluid Mechanics, Braunschweig, 36 (1992).

[7] J.-L. GUERMOND, C. MIGEON, G. PINEAU AND L. QUARTAPELLE, *Start-up flows in a three-dimensional rectangular driven cavity of aspect ratio* $1:1:2$ *at* $Re = 1000$, J. Fluid Mech., 450 (2002), pp. 169–199.

[8] J.-L. GUERMOND AND J. SHEN, *A new class of truly consistent splitting schemes for incompressible flows*, J. Comput. Phys., 192 (2003), pp. 262–276.

[9] Y. KATO, H. KAWAI AND T. TANAHASHI, *Numerical flow analysis in a cubic cavity by the GSMAC finite element method*, JSME Int. J. Ser. II, 33 (1990), pp. 649–658.

[10] J. R. KOSEFF AND R. L. STREET, *The lid-driven cavity flow: A synthesis of qualitative and quantitative observations*, ASME J. Fluids Eng., 106 (1984), pp. 390–398.

[11] J. R. KOSEFF, R. L. STREET, P. M. GRESHO, C. D. UPSON, J. A. C. HUMPHREY AND W. M. TO, *A three-dimensional lid-driven cavity flow: experiment and simulation*, Proc. Third Int. Conf. on Numerical Methods in Laminar and Turbulent Flows, Seattle, 1983, pp. 564–581.

[12] C. MIGEON, *Details on the start-up development of the Taylor-Görtler-Like vortices inside a square-section lid-driven cavity for* $1000 \leq Re \leq 3200$, Exp. Fluids, 33 (2002), pp. 594–602.

[13] J. SHEN AND X. F. YANG, *Error estimates for finite element approximations of consistent splitting schemes for incompressible flows*, Discrete Cont. Dyn.-B, 8 (2007), pp. 663–676.

[14] B. C. SHI AND H. F. HAN, *Parallel lattice BGK simulations of three-dimensional lid-driven cavity flow*, in: WCCM VI in conjunction with APCOM' 04, Sept. 5–10, 2004, Beijing, China.

[15] K. L. WONG AND A. J. BAKER, *A modular collaborative parallel CFD workbench*, J. Supercomput., 22 (2002), pp. 45–53.